Acta Materialia 309 (2026) 122070

Contents lists available at ScienceDirect

Acta Materialia

journal homepage: www.elsevier.com/locate/actamat

Full length article

Atomic-Insights into electron-beam irradiation-induced degradation in all-inorganic metal halide perovskites

Qingye Zhang [a,1], Feiyu Diao [b,1], Rongsheng Cai [c,*], Guangwen Zhou [d,*], Yiqian Wang [a,*]

[a] College of Physics, Qingdao University, No. 308 Ningxia Road, Qingdao, 266071, PR China
[b] Industrial Research Institute of Nonwovens & Technical Textiles, Shandong Center for Engineered Nonwovens, College of Textiles & Clothing, Qingdao University, No. 308 Ningxia Road, Qingdao, 266071, PR China
[c] State Key Laboratory of Solid Lubrication, Lanzhou Institute of Chemical Physics, Chinese Academy of Sciences, Lanzhou, 730000, PR China
[d] Department of Mechanical Engineering & Materials Science and Engineering program, State University of New York, Binghamton, NY, 13902, USA

ARTICLE INFO

Keywords:
Cesium lead halide
In-situ STEM
Electron beam irradiation
Degradation mechanism
Endotaxial growth

ABSTRACT

The operational stability of all-inorganic perovskites $CsPbX_3$ (X = Cl, Br, I) remains a bottleneck in advancing their use in optoelectronics and space-based photovoltaics. A key challenge lies in understanding their degradation under high-energy radiation, which is poorly characterized at the atomic scale, largely because conventional high-resolution characterization techniques often induce structural damage they aim to probe. Herein, we address this challenge by employing an edge-view imaging geometry *in-situ* scanning-transmission electron microscopy, enabling direct atomic-scale visualization of radiation-induced degradation in orthorhombic $CsPbBr_3$ under controlled electron-beam irradiation. This cross-sectional approach reveals a previously unrecognized degradation pathway: the endotaxial nucleation and growth of metallic Pb nanocrystals within the perovskite matrix, characterized by Pb {111} planes parallel to $CsPbBr_3$ {022}/{202} planes and twinning along Pb {111} planes during growth. Complementary density functional theory calculations show that interfacial Pb atomic layers energetically stabilize this epitaxial alignment, thereby directing the endotaxial growth process. These results reveal the atomic-scale mechanisms governing radiation-induced degradation in $CsPbX_3$ perovskites, which offer broad insights for designing radiation-resistant perovskite-based devices such as space solar cells and for interpreting beam-induced effects in radiation-sensitive semiconductors.

1. Introduction

All-inorganic metal halide perovskites, particularly cesium lead halide perovskites ($CsPbX_3$, X = Cl, Br, I), have attracted significant attention over the past decade due to their exceptional optical and electronic properties, positioning them as promising materials for next-generation optoelectronic devices, including solar cells, light-emitting diodes (LEDs), photodetectors, lasers, and luminescent solar concentrators (LSCs) [1–6]. Despite their remarkable performance, the widespread application of $CsPbX_3$-based devices is severely limited by their intrinsic instability under external environmental stimuli, such as heat, moisture, and irradiation [7–12]. Among these, irradiation-induced degradation is particularly critical. Specifically, when the $CsPbX_3$-based devices are used for space solar cells, irradiation often induces a series of detrimental changes, including structural phase transition, defect formation, and the segregation of constituent elements into distinct phases. Notably, the formation of lead (Pb) nanoparticles is a prominent feature of these changes [13–17] These Pb nanoparticles can perturb the local electronic structure, introduce additional scattering centers, and alter carrier dynamics, ultimately compromising device efficiency and operational stability. Therefore, understanding the mechanisms underlying irradiation-driven degradation of $CsPbX_3$ at atomic scale is essential for designing radiation-resistant perovskite-based solar cells suitable for space missions.

Advanced characterization techniques, in particular high-resolution transmission electron microscopy (HRTEM), are essential for elucidating the structural transformation and decomposition products of $CsPbX_3$ [13–18]. For instance, Manna et al. [13]. investigated the effect of high-energy electron-beam irradiation on $CsPbBr_3$ nanosheets, nanowires, and nanocubes, demonstrating that electron beams could

* Corresponding authors.
E-mail addresses: rongshengcai@licp.cas.cn (R. Cai), gzhou@binghamton.edu (G. Zhou), yqwang@qdu.edu.cn (Y. Wang).
[1] These authors contributed to this work equally.

https://doi.org/10.1016/j.actamat.2026.122070
Received 18 November 2025; Received in revised form 7 February 2026; Accepted 2 March 2026
Available online 3 March 2026

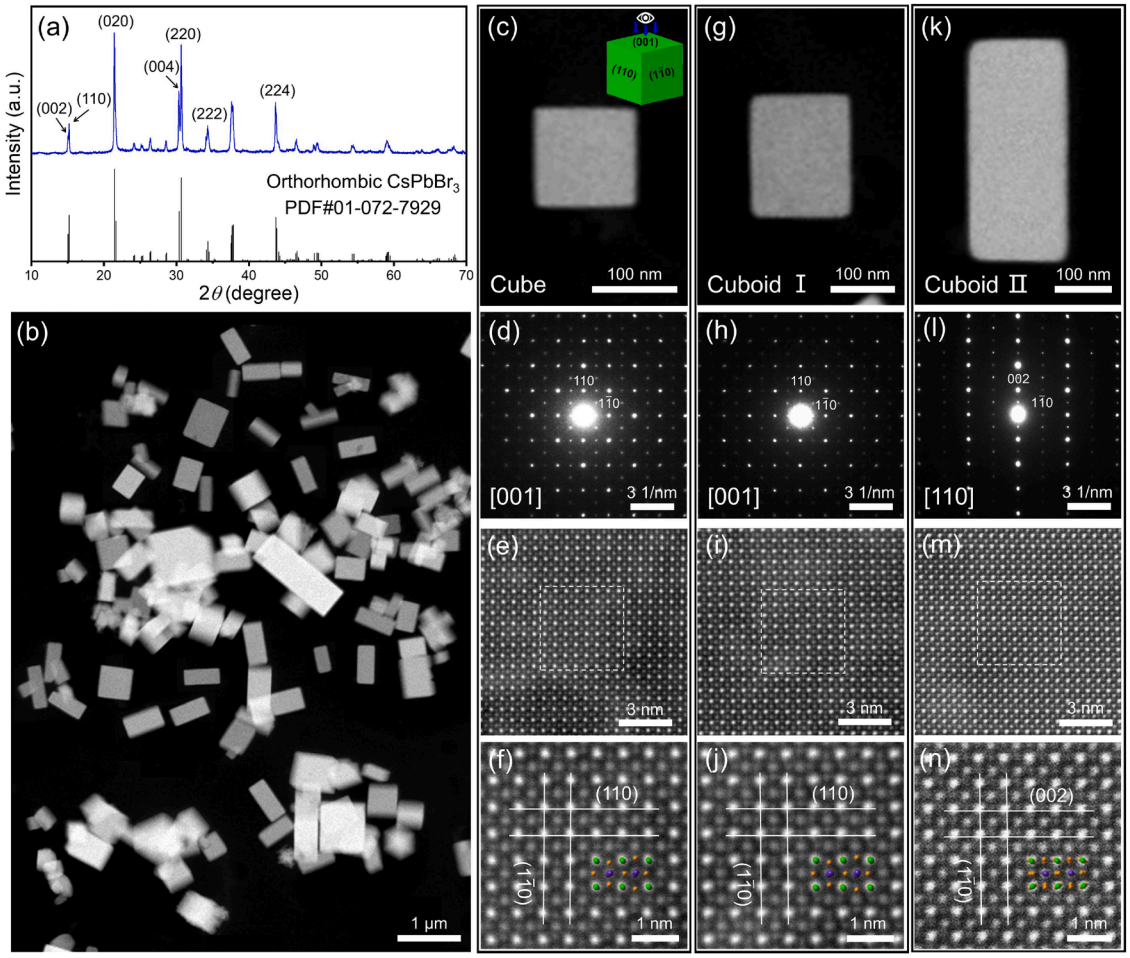

Fig. 1. Structural characterization of $CsPbBr_3$ nanocrystals. (a) XRD pattern of the as-synthesized products. (b) Typical low-magnification STEM image of $CsPbBr_3$ particles. Typical STEM images, together with the corresponding SAED patterns and aberration-corrected HAADF images for (c-f) $CsPbBr_3$ cube, (g-j) $CsPbBr_3$ cuboid I, (k-n) $CsPbBr_3$ cuboid II. Insets in (f,j,n) show atomic models of orthorhombic $CsPbBr_3$, viewed from different directions, where purple, green, and orange spheres represent Cs, Pb and Br atoms, respectively.

induce the nucleation and growth of Pb nanoparticles. Similar observations were reported by Wang et al. [14]., further confirming formation of metallic Pb under electron-beam irradiation. In addition to Pb, other studies have identified formation of CsX nanoparticles. Manna et al. [15]. examined the impact of electron-beam irradiation on $CsPbBr_3$ nanosheets and nanocubes under low-temperature (≤ -40 °C) conditions, and observed the formation of CsBr, CsPb, and $PbBr_2$ on the surfaces of nanosheets and nanocubes. Diao et al. [16]. employed *in-situ* HRTEM to study the degradation behaviors of $CsPbBr_3$ nanobricks with different thicknesses under electron-beam irradiation. It is revealed that thick $CsPbBr_3$ nanobricks undergo decomposition, leading to formation of Pb and CsBr nanoparticles, whereas thin nanobricks decompose into amorphous Pb. Likewise, metallic Pb and Cs_2IBr nanoparticles were observed on the surface of $CsPbIBr_2$ films subjected to electron-beam irradiation [17]. Despite these insights, *in-situ* atomic-resolution studies of irradiation-induced degradation are still limited. This is primarily ascribed to the high sensitivity of all-inorganic metal halide perovskites to electron beam. Although these materials are generally more stable than the organic-inorganic hybrid counterparts, prolonged exposure to high-dose electron irradiation still causes rapid degradation, severely hindering atomic-resolution imaging and leaving critical gaps in understanding their microstructural evolution.

Recently, integrated differential phase-contrast scanning-transmission electron microscopy (iDPC-STEM) has enabled low-dose, atomic-scale imaging of $CsPbI_3$ quantum dots, resolving local structures such as surfaces and interfaces [19]. Despite these advances, key questions remain regarding the dynamic processes governing Pb-nanoparticle formation during irradiation-induced degradation of $CsPbBr_3$, including identification of initial nucleation sites, growth kinetics, and interactions with the surrounding $CsPbX_3$ lattice. Without atomic-level insights, understanding the fundamental mechanisms of irradiation-induced degradation and designing more robust and efficient $CsPbX_3$-based optoelectronic devices remains challenging.

In this work, orthorhombic $CsPbBr_3$ nanocrystals were synthesized using a slightly-adapted room-temperature supersaturated recrystallization (SR) method. Atomic-resolution imaging was employed to probe their microstructure and surface characteristics. *In-situ* STEM observations from an edge-view geometry were performed to investigate the degradation pathways of $CsPbBr_3$ nanocrystals under electron-beam irradiation, revealing that Pb nanoparticles form through endotaxial growth. Density functional theory (DFT) calculations further confirmed the oriented growth of Pb nanoparticles and elucidated the atomic-scale interfacial interactions stabilizing this process. Collectively, these findings provide critical insights into the irradiation-induced degradation mechanisms of $CsPbX_3$ and offer guidance for the rational design of more robust perovskite-based optoelectronic devices.

2. Methods

2.1. Synthesis of $CsPbBr_3$ nanocrystals

$CsPbBr_3$ nanocrystals were synthesized by a slightly modified room-

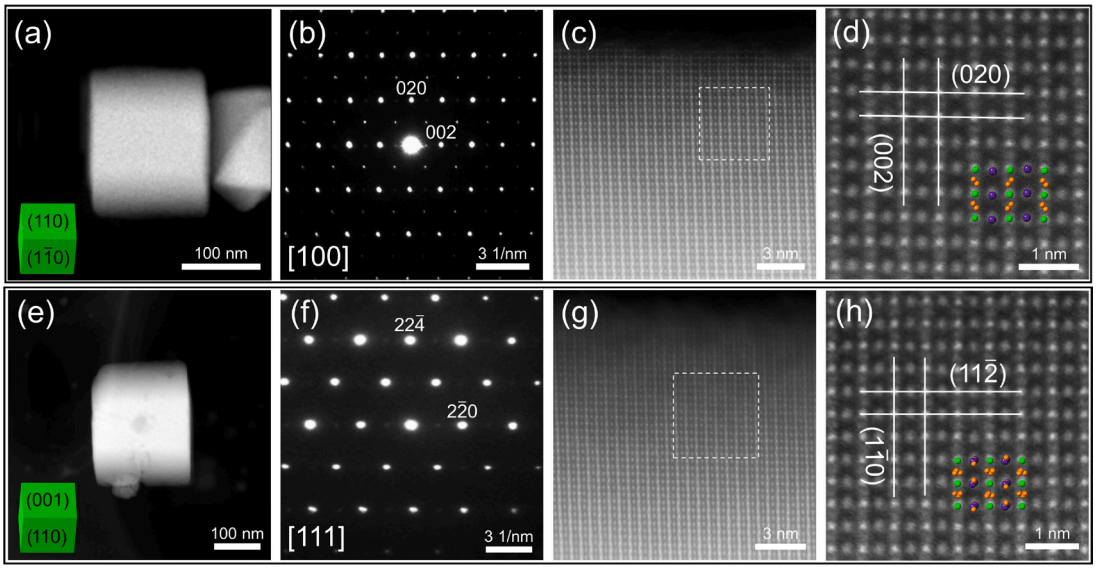

Fig. 2. Edge-view images of $CsPbBr_3$ nanocrystals. Typical STEM images, the corresponding SAED patterns and aberration-corrected HAADF images for $CsPbBr_3$ cubes observed from edges along the (a-d) [100] and (e-h) [111] zone-axes. Insets in (d,h) show atomic models of orthorhombic $CsPbBr_3$, viewed from different directions, where purple, green, and orange spheres represent Cs, Pb and Br atoms, respectively.

temperature SR approach. Briefly, 0.15 mmol of CsBr (99.5 %) and 0.15 mmol of $PbBr_2$ (90.0 %) were dissolved in 3.5 mL of *N, N*-Dimethylformamid (DMF, 99.5 %) by stirring in air at 30 °C for 1 h to form a clear precursor solution. Subsequently, 200 μL of oleic acid (90.0 %) and 50 μL of oleylamine (90.0 %) were added into the precursor solution. Under continuous stirring, 10 mL of ethanol was rapidly added, leading to a color change from transparent to orange-yellow. The resulting crude nanocrystals were centrifuged at 1500 rpm for 5 min. The supernatant was then removed, and the remaining solution was centrifuged at 10,000 rpm for 10 min. The obtained products were washed by centrifugation three times and then re-dispersed in hexane.

2.2. Structural characterization

X-ray diffraction (XRD) patterns were recorded using a Rigaku SmartLab SE apparatus with Cu-Kα_1 radiation ($\lambda = 1.5406$ Å). Selected-area electron diffraction (SAED), STEM or high-angle annular dark field (HAADF) imaging, and energy-dispersive X-ray spectroscopy (EDS) elemental mapping were performed on a Thermo Scientific Spectra 300 (S)TEM operating at 300 kV.

2.3. Computation methods

All calculations were carried out using the CASTEP program package in Material Studio [20]. The Perdew-Burke-Ernzerhof (PBE) functional within the generalized gradient approximation (GGA) was employed for the exchange-correlation potential [21]. Structural optimizations were performed with a plane-wave cutoff energy of 220 eV and a *k*-point mess with a resolution of $2\pi \times 0.05$ Å^{-1}. Convergence criteria were set such that the total energy change was less than 0.02 meV atom^{-1}, and the maximum force on each atom was below 0.03 eV Å^{-1}, and the maximum atomic displacement was less than <0.005 Å.

3. Results and discussion

3.1. Structural and morphological characterization of $CsPbBr_3$ nanocrystals

The crystal structure of the synthesized $CsPbBr_3$ nanocrystals was examined using XRD. As shown in Fig. 1a, the diffraction peaks match well with orthorhombic $CsPbBr_3$ (PDF#01–072–7929, $a = 8.207$ Å, $b = 8.255$ Å, $c = 11.759$ Å, $\alpha = \beta = \gamma = 90°$), with no detectable impurities. Fig. 1b presents a low-magnification STEM image of the product, revealing that the nanoparticles have three main dominant morphologies: cube, cuboid I, and cuboid II. Particles with an aspect ratio close to 1 are defined as cubes, those with an aspect ratio of ~1.5 as cuboid I, and those with an aspect ratio greater than 2 as cuboid II. Statistical analysis of particle distribution (Table S1) shows that cubes, cuboid I, and cuboid II account for approximately 19.4 %, 34.4 %, and 46.2 % of the whole nanoparticles, respectively.

Fig. 1c, g and k present typical STEM images of individual $CsPbBr_3$ particles representing various morphologies (cubes, cuboid I, and cuboid II). The corresponding SAED patterns are illustrated in Fig. 1d, h and l, respectively. These SAED patterns can be indexed as [001], [001], and [110] zone axes of orthorhombic $CsPbBr_3$. HAADF imaging clearly resolves the elemental distribution within the nanocrystals. In these aberration-corrected HAADF images, the image contrast scales approximately with the atomic number Z as $Z^{1.67}$, so heavier elements appear brighter: Pb as the brightest, Cs as the second-brightest, and Br as the darkest.

Detailed examination of the HAADF images shows that, in cubes (Fig. 1f), the observed crystal planes correspond to (110) and (1$\bar{1}$0) of orthorhombic $CsPbBr_3$ with an interplanar spacing of 5.82 Å and an angle of 90°, viewed along the [001] direction. Cuboid I (Fig. 1j) exhibits similar plane orientations. For cuboid II (Fig. 1n), the interplanar spacings are measured to be 5.88 Å and 5.82 Å, corresponding to the (002) and (1$\bar{1}$0) planes of orthorhombic $CsPbBr_3$, observed along the [110] direction. Although the [001] and [110] zone axes produce similar Pb and Cs atomic patterns, the Br atom distribution allows unambiguous distinction: along the [001] direction, Br atoms form rhombic arrangements with alternating orientations, whereas along the [110] direction, Br atoms form nearly square arrangements, as illustrated in the corresponding atomic models in Fig. 1f, j and n. Atomic models of orthorhombic $CsPbBr_3$, viewed along the [001], [110], [100], and [111] directions, are shown in Fig. S1.

Based on morphological analysis and high-resolution atomic imaging, the exposed surfaces of all three types of $CsPbBr_3$ nanocrystals, cube, cuboid I and cuboid II, are predominantly {001} and {110} crystal facets. This assignment is consistent with previous reports, indicating that the {001} and {110} faces of orthorhombic $CsPbBr_3$ are low-energy surfaces [22–25]. For the $CsPbBr_3$ cubes, in addition to the top-view

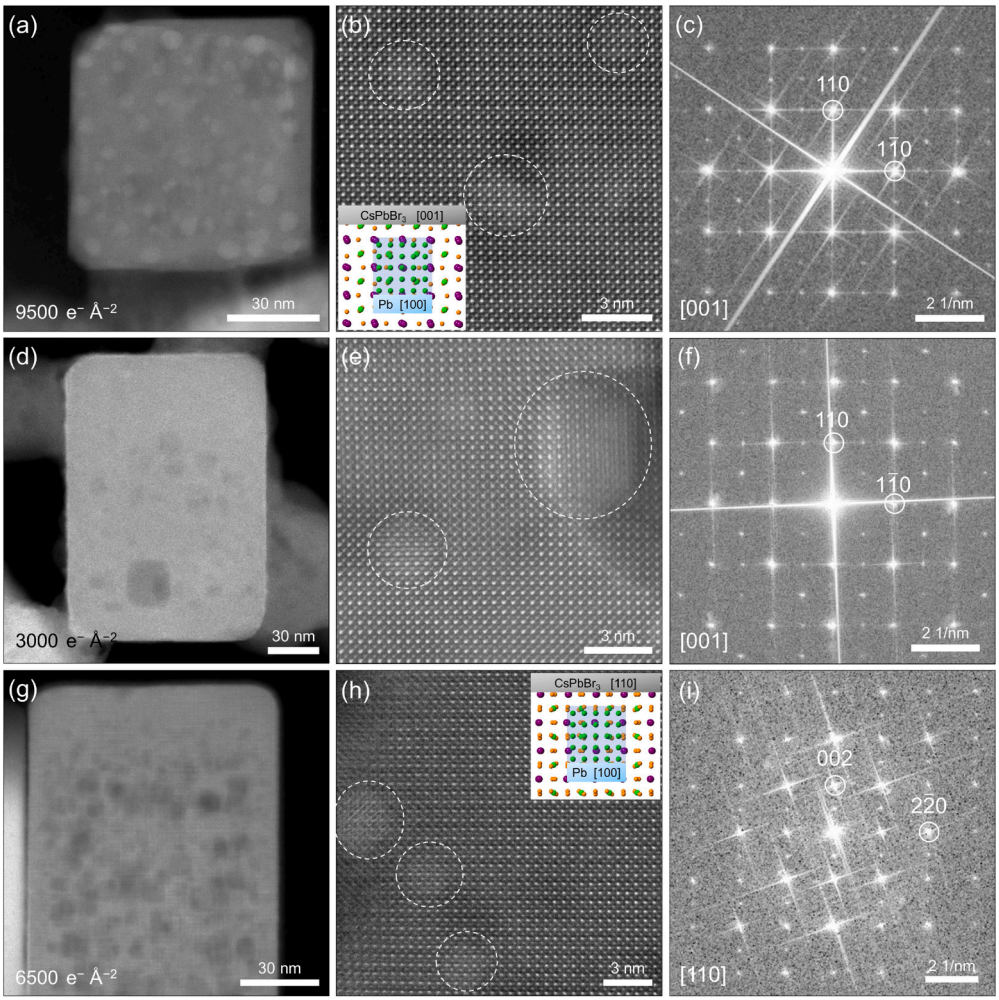

Fig. 3. Electron-beam irradiation-induced decomposition of $CsPbBr_3$ nanocrystals. Aberration-corrected HAADF images of $CsPbBr_3$ (a) cube, (d) cuboid I and (g) cuboid II after electron-beam irradiation. Corresponding enlarged HAADF images of $CsPbBr_3$ (b) cube, (e) cuboid I and (h) cuboid II. Corresponding FFT patterns of $CsPbBr_3$ (c) cube, (f) cuboid I and (i) cuboid II. Insets are the atomic models of overlapping views for the parent $CsPbBr_3$ lattices and the newly-formed Pb particle.

along the [001] zone axis (Fig. 1c-f), a side-view along the [110] zone axis is present in Fig. S2. However, it is challenging to observe cuboid I along [110] and cuboid II along [001] due to their anisotropic shapes and morphological characteristics. As shown in Fig. S3, the small $CsPbBr_3$ cube ("seed crystal") exposes two {001} faces and four {110} faces. Because the surface energies of {001} and {110} facets are comparable [23], these seed crystals can assemble through different faces: assembly through both {110} and {001} faces produces larger cubes, enabling STEM imaging along the [001] and [110] zone axes. Assembling predominantly through {110} faces forms cuboid I, which resembles nanosheets with minimal thickness along the [001] direction; consequently, only HAADF images along the [001] zone axis can be obtained. Conversely, assembly primarily through {001} faces yields cuboid II, for which only HAADF images along the [110] zone axis can be observed due to its elongated shape. Schematic illustrations of different self-assembly pathways, demonstrating the transformation from seed crystals into cube, cuboid I, and cuboid II, are presented in Fig. S4.

During extensive STEM observations, $CsPbBr_3$ cubes were examined not only from the top view but also from the edge view. In the top-view image (Fig. 1c), the contrast is homogeneous, whereas in the edge-view images (Fig. 2a, e), the middle region shows brighter contrast than the upper and lower edges. This suggests that the edge is thinner than the middle region, which is more suitable for SAED and HAADF observations. The SAED (Fig. 2b, f) and HAADF images (Fig. 2c, g), obtained from the upper edges, can be indexed as [100] and [111] zone axes of orthorhombic $CsPbBr_3$. The SAED patterns of these two edge-oriented $CsPbBr_3$ cubes exhibit prominent differences, providing clear and definitive evidence for accurately identifying their respective zone axes. In contrast, distinguishing between the [100] and [111] zone axes based solely on HAADF images is more challenging, as the Pb and Cs atom arrangements appear very similar, as illustrated in the atomic models in Fig. S1c, d. Furthermore, the measured interplanar distances are also very close. In the magnified HAADF image in Fig. 2d, the interplanar distances of 4.13 Å and 5.88 Å correspond to the (020) and (002) planes, respectively, of orthorhombic $CsPbBr_3$. In Fig. 2h, the measured interplanar spacings of 4.14 Å and 5.82 Å correspond to the (11$\bar{2}$) and (1$\bar{1}$0) planes. The near equivalence of these spacings, (020) *vs.* (11$\bar{2}$), (002) *vs.* (1$\bar{1}$0), makes it difficult to distinguish between the [100] and [111] zone axes based only on the interplanar spacings. Thus, the SAED patterns serve as the most reliable method for unambiguously differentiating the [100] and [111] zone axes of orthorhombic $CsPbBr_3$.

3.2. *Electron-beam irradiation-induced decomposition pathways of $CsPbBr_3$ nanocrystals*

In-situ TEM, with its unique capability for real-time observation, has been widely applied to the study of the stability of $CsPbX_3$ nanomaterials. In our experiments, $CsPbBr_3$ nanocrystals exhibiting multiple orientations, combined with high-resolution STEM imaging technique,

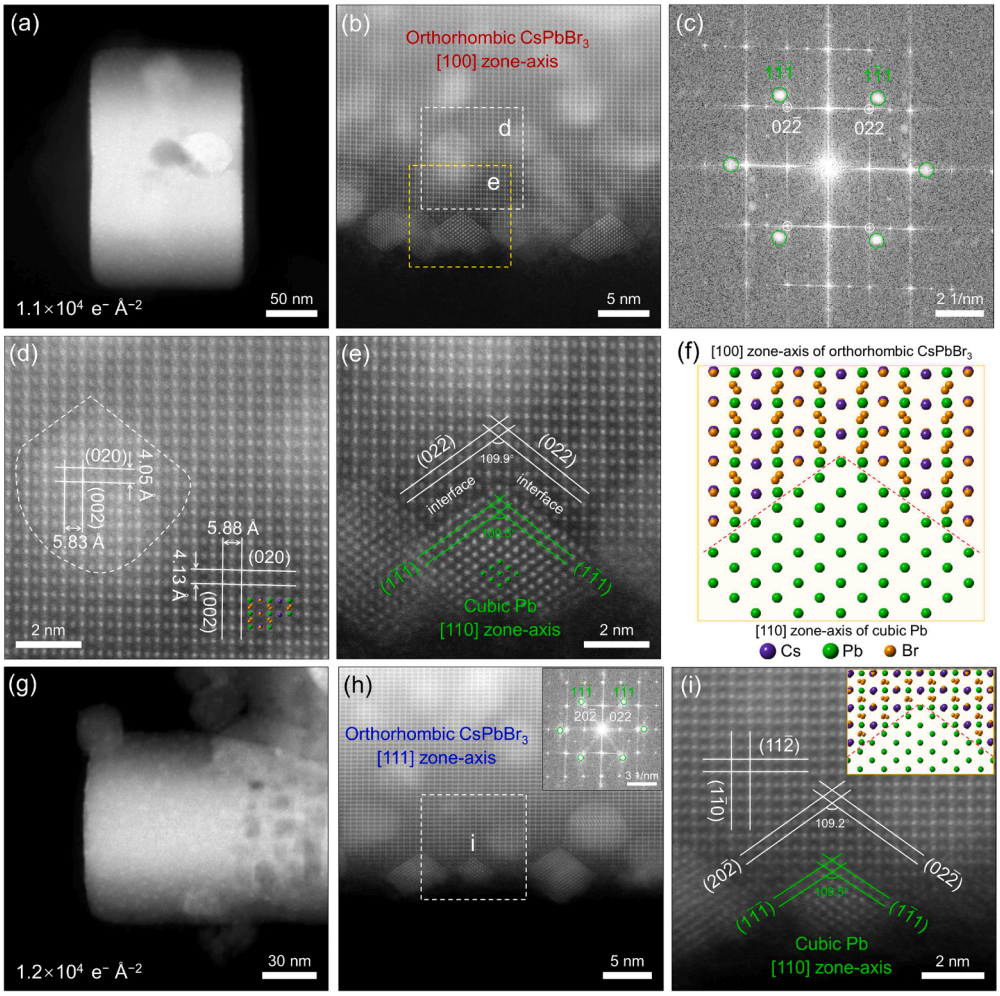

Fig. 4. STEM observations of damaged $CsPbBr_3$ nanocrystals from the edge view. (a and g) Aberration-corrected HAADF image of edge-oriented $CsPbBr_3$ particles after electron-beam irradiation. (b) Enlarged HAADF image from (a). (c) FFT pattern corresponding to (b). (d and e) Enlarged HAADF images of the regions enclosed by the white and yellow squares in (b), respectively. (f) Atomic model schematic illustrating the interface between $CsPbBr_3$ and the newly-formed Pb, corresponding to (e). (h) Enlarged HAADF image from (g), with an inset showing the corresponding FFT pattern. (i) Enlarged HAADF image of the region enclosed by the white square in (h), with an inset showing the corresponding schematic atomic model of the interface structure.

offer an ideal platform for investigating their decomposition behaviors. It is well-established that $CsPbX_3$ nanomaterials degrade under electron-beam irradiation, typically manifested by formation of bright-contrast nanoparticles on their surfaces, as seen in Fig. 3a, d, and g. Detailed examination of the HAADF images (Fig. 3b, e, h), viewed along [001] and [110], reveals that bright-contrast particles with a circular shape, outlined by white dashed lines, are significantly brighter than the host $CsPbBr_3$ lattice. This brighter contrast arises from beam-induced decomposition of $CsPbBr_3$, leading to the aggregation of Pb on the $CsPbBr_3$ surface [13,16]. More STEM examinations (Fig. S5) show that Pb nanoparticles can also form in the edge region, with a shape similar to those observed on the $CsPbBr_3$ surface.

The corresponding fast Fourier transform (FFT) patterns (Fig. 3c, f, i), indexed as the [001], [001], and [110] zone axes of orthorhombic $CsPbBr_3$, show that diffraction information from Pb is not readily detectable due to the extremely small size of the newly-formed Pb nanocrystals. Moreover, when viewed along the top-down perspective of the $CsPbBr_3$ cube, cuboid I and cuboid II, the lattices of the base $CsPbBr_3$ overlap with those of the newly-formed Pb nanocrystals. This overlap, caused by the finite thickness of the $CsPbBr_3$ nanocrystals, complicates the real-time identification of degradation pathways along the [001] or [110] zone axes, and makes it hard to determine the orientation relationship between $CsPbBr_3$ and the newly-formed Pb particles. In addition, the top-down perspective might even render misleading information about the growth mode and shape of the formed Pb nanoparticles.

From extensive STEM examinations, it is found that the edge-oriented $CsPbBr_3$ particles with distinct edges (as shown in Fig. 2a, e) offer a clear perspective for probing their decomposition behaviors, which is ascribed to the fact that the edges are thinner than the other regions when viewed from certain directions, and degrade more easily under electron-beam irradiation[16]. As shown in Fig. 4a, a large number of brighter nanoparticles appear on the surface of $CsPbBr_3$ particles after electron-beam irradiation, with a particular high density along the edges. The enlarged HAADF image (Fig. 4b) clearly reveals that these nanoparticles adopt specific orientation relationship with the $CsPbBr_3$ lattices. It is noteworthy that the morphology of these Pb nanocrystals seems to vary in different regions, as shown in Fig. S6. In the edge region, most Pb particles manifest as regular triangles, while in the central region some Pb nanocrystals display irregular shapes. This morphological variation is associated with the sample thickness at different regions. Compared to the edge region, the central region is much thicker. In the central region, the nucleation sites are denser and the coalescence of adjacent Pb nanocrystals happens more easily, thus leading to appearance of irregular shapes. The corresponding FFT pattern (Fig. 4c) confirms this observation: the diffraction spots marked

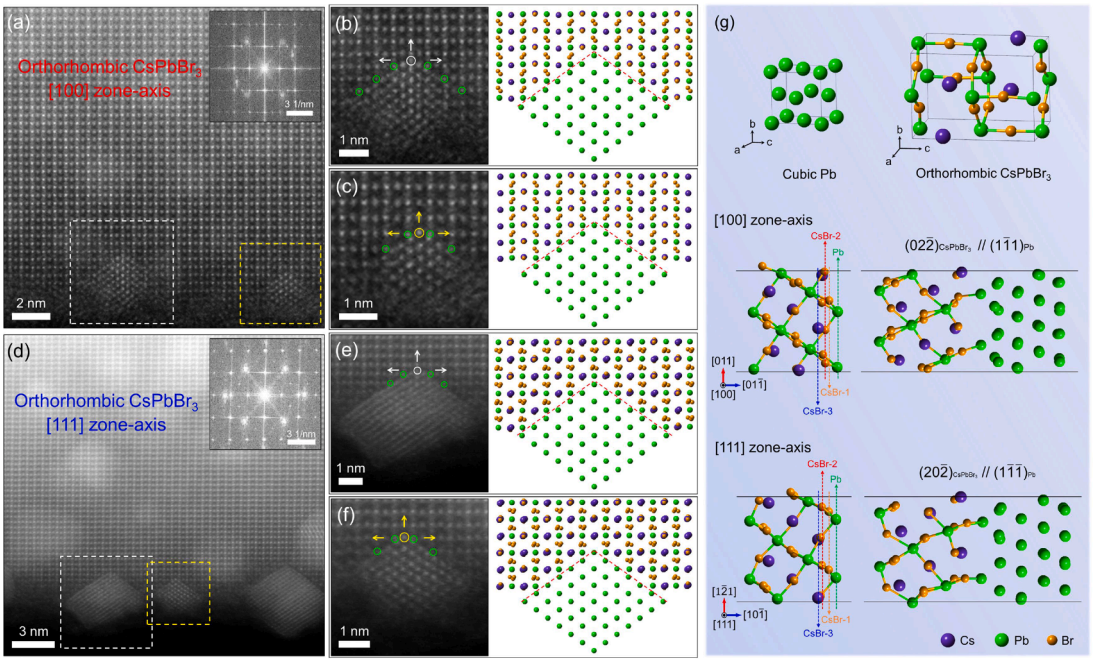

Fig. 5. Interface structure between host $CsPbBr_3$ and newly-formed Pb nanoparticles. Partially enlarged HAADF images of $CsPbBr_3$ particles along the (a) [100] and (d) [111] zone-axes after electron-beam irradiation, with insets showing the corresponding FFT patterns. Enlarged HAADF images of the region enclosed by the (b and e) white and (c and f) yellow squares in (a and d) respectively, with the corresponding atomic models shown on the right of each HAADF image. (g) Schematic illustrations of the Pb unit cell (space group *Fm*$\bar{3}$*m*) and the $CsPbBr_3$ unit cell (space group *Pbnm*) with $CsPbBr_3$ atomic layers stacking along the [01$\bar{1}$] and [10$\bar{1}$] directions, and the corresponding $CsPbBr_3$-Pb interfaces with the lowest energy.

by white circles can be indexed to the {022} planes of orthorhombic $CsPbBr_3$ along the [100] zone axis, while the additional diffraction spots marked by green circles correspond to the {111} planes of cubic Pb viewed along the [110] zone axis. In contrast to the decomposition behavior reported by Shen *et al.* [26], our STEM observations reveal the lattice signatures only corresponding to $CsPbBr_3$ and Pb. This indicates that no intermediate phases, such as $PbBr_2$ or CsBr, form under our experimental conditions (incident electron energy of 300 keV, dose rate of 650 e^{-1} $Å^{-2}$ s^{-1}). The absence of these intermediates is attributed to the rapid displacement of Br atoms from the $CsPbBr_3$ lattice under the electron-beam irradiation, likely driven by knock-on collisions [16], which promotes the direct reduction of Pb^{2+} into Pb. To further confirm the composition of the decomposition products, EDS mapping was performed on the irradiated regions (Fig. S7). The elemental mappings are consistent with the $CsPbBr_3$ framework, but they also show strong Pb intensity at the nanoparticle locations. This confirms that the newly-formed nanoparticles with a high contrast are composed of Pb, in agreement with the previous reports [13,16].

Closer inspection of the region highlighted by a white square in Fig. 4b provides further insights. In the darker-contrast region (Fig. 4d), the measured interplanar spacings are 4.13 Å and 5.88 Å, corresponding to the (020) and (002) planes of orthorhombic $CsPbBr_3$, consistent with the analysis results from Fig. 2d By contrast, the brighter-contrast area enclosed by the white dashed lines shows slightly-reduced interplanar spacings of 4.05 Å and 5.83 Å. This suggests that the Pb atoms lost from the base $CsPbBr_3$ lattices accumulate in the bright-contrast region, leading to the lattice shrinkage of base $CsPbBr_3$.

To establish the orientation relationship between $CsPbBr_3$ and Pb, a detailed analysis of the interfacial structures was performed (Fig. 4e). For the undamaged portion of the $CsPbBr_3$ lattices, two planes are identified: (02$\bar{2}$) and (022) planes, both with an interplanar spacing of 3.38 Å and an angle of 109.9° For the Pb nanoparticles, an interplanar spacing of 2.86 Å and an angle of 109.5° is measured, corresponding to the {111} planes of cubic Pb. Fig. 4f shows the atomic model of the $CsPbBr_3$-Pb interface derived from the above analysis. Consequently, the orientation relationships between $CsPbBr_3$ and Pb, when viewed along the [100] zone axis of orthorhombic $CsPbBr_3$, are determined as follows.

$$[100]CsPbBr_3//[110]Pb \quad (1)$$

$$(02\bar{2})CsPbBr_3//(1\bar{1}1)Pb \quad (2)$$

$$(022)CsPbBr_3//(1\bar{1}1)Pb \quad (3)$$

We further examined the edge-oriented $CsPbBr_3$ particles along the [111] zone axis after the electron-beam irradiation, as shown in Fig. 4*g*-i. The inset FFT pattern in Fig. 4h confirms that the particle is oriented along the [111] zone axis of orthorhombic $CsPbBr_3$. The diffraction spots marked by white circles can be indexed as the {20$\bar{2}$} and {02$\bar{2}$} planes of orthorhombic $CsPbBr_3$, while the additional diffraction spots marked by green circles correspond to the {111} planes of cubic Pb. In Fig. 4i, in addition to the (11$\bar{2}$) and (1$\bar{1}$0) planes of orthorhombic $CsPbBr_3$, two additional planes separated by 109.2° are observed. The measured interplanar spacings of 3.37 Å and 3.38 Å agree well with those of the (20$\bar{2}$) and (02$\bar{2}$) planes of orthorhombic $CsPbBr_3$. For the Pb nanoparticles, the structural features are consistent with the results obtained from Fig. 4e. The inset in Fig. 4i shows the corresponding atomic model of the $CsPbBr_3$-Pb interface. From the above analysis, the orientation relationships between $CsPbBr_3$ and Pb, when viewed along the [111] zone axis of orthorhombic $CsPbBr_3$, can be deduced as follows.

$$[111]CsPbBr_3//[110]Pb \quad (4)$$

$$(20\bar{2})CsPbBr_3//(1\bar{1}1)Pb \quad (5)$$

$$(02\bar{2})CsPbBr_3//(1\bar{1}1)Pb \quad (6)$$

Comparing the orientation relationships (1) to (6), it becomes clear that the orientation relationship consistently occurs between the {111} facets of cubic Pb and the {022}/{202} facets of orthorhombic $CsPbBr_3$. The growth of Pb nanoparticles thus exhibits characteristic endotaxial growth behavior [27]. Specifically, this is enabled by two factors: (i) the

Table 1
Formation energies of point defects in $CsPbBr_3$ obtained by DFT calculations.

Point defect	Formation energy (eV)
V_{Cs}	−3.51
V_{Pb}	3.36
V_{Br}	0.69

high lattice matching between the {111} planes of cubic Pb and {022}/{202} planes of orthorhombic $CsPbBr_3$[28], and (ii) the thermodynamic stability of the {111} planes of cubic Pb as the lowest-energy facets[29]. Together, these factors provide both crystallographic compatibility and surface energy advantage, promoting the endotaxial embedding of Pb nanoparticles within the $CsPbBr_3$ lattices. This crystallographic matching, coupled with interface energy minimization, not only explains the orientation-controlled growth of Pb nanocrystals, but also clarifies the mechanism underlying the preferential decomposition of $CsPbBr_3$ nanocrystals in the edge regions. In addition to the high density of dangling bonds and surface defects at the edge sites, the preferential nucleation and growth of cubic Pb nanocrystals at the low-coordination edge sites are also an important factor that accelerates the decomposition of $CsPbBr_3$ nanocrystals.

To gain deeper insight into the interface structure between $CsPbBr_3$ and Pb nanocrystals, detailed STEM examinations were performed. Fig. 5a presents a typical HAADF image of a damaged $CsPbBr_3$ particle. The corresponding FFT pattern (inset) confirms that this particle orients along the [100] zone axis of orthorhombic $CsPbBr_3$. Two Pb nanocrystals are observed at the particle edge. Although both Pb nanocrystals share the same overall orientation relationships with the $CsPbBr_3$ crystal, subtle differences in their atomic arrangements at the interface are apparent. Magnified HAADF images and corresponding atomic models are shown in Fig. 5b, c. In Fig. 5b, the topmost Pb atom (enclosed by a white circle) aligns with the PbBr layer of $CsPbBr_3$ along the vertical direction (indicated by the upward white arrow) and Br layer along the horizontal direction (labeled by the horizontal white arrows). In contrast, in Fig. 5c, the topmost Pb atom enclosed by the yellow circle aligns with the Cs layer vertically (indicated by the upward yellow arrow) and the PbBr layer horizontally (marked by the horizontal yellow arrows). In both cases, a layer of Pb atoms is present at the interface, indicated by the green circles, which can be proved by the corresponding atomic models. Notably, the atomic contrast at these positions is darker than that of Pb atoms within the $CsPbBr_3$ lattices, suggesting that Pb atoms in the adjacent $CsPbBr_3$ lattice are consumed during the endotaxial growth of Pb nanocrystals. Consequently, the observed atomic contrast originates from deeper Pb atoms within the $CsPbBr_3$ lattice along the STEM observation direction. Similar phenomena are observed along the [111] zone axis of orthorhombic $CsPbBr_3$, as shown in Fig. 5d-f. These observations indicate that, regardless of whether the interface is viewed along the [100] or [111] zone axis, the outermost atomic layer of $CsPbBr_3$ at the interface is primarily composed of Pb atoms.

The formation of unique interfacial structures between $CsPbBr_3$ and Pb is further supported by DFT calculations. For the interface simulations, the $(01\bar{1})$ and $(10\bar{1})$ planes of $CsPbBr_3$ were chosen to combine with the (111) plane of Pb, based on the orientation relationships observed in Fig. 5a, d. For Pb, only one type of (111) plane was considered, while for $CsPbBr_3$, four types of $(01\bar{1})$ and four types of $(10\bar{1})$ termination layers were selected (Fig. 5g), resulting in eight possible interface structures depending on the $CsPbBr_3$ termination plane. Schematics of these optimized interface structures are shown in Fig. S9, and the corresponding interface energies are summarized in Table S2. The calculation results indicate that, for both the $(01\bar{1})$ and $(10\bar{1})$ planes of $CsPbBr_3$, the interface energy is lowest when terminated by Pb atomic layers, in good agreement with our STEM observations.

Furthermore, the formation energies of point defects in the orthorhombic $CsPbBr_3$ were also calculated, and the results are summarized in Table 1. The corresponding calculation details can be found in the SI. The results indicate that Cs atoms have the lowest point-defect formation energy, suggesting that Cs atoms preferentially detach from the lattice during the degradation, consistent with the previous report [30].

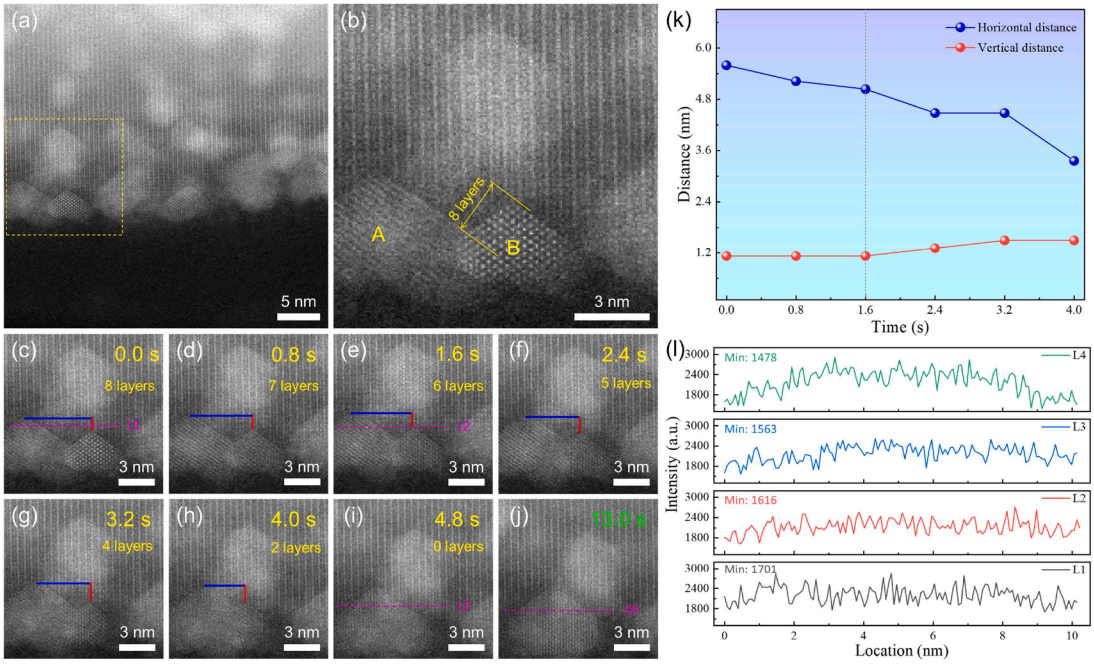

Fig. 6. Morphological evolution of Pb nanoparticles in an individual $CsPbBr_3$ nanocrystal under electron-beam irradiation (dose rate: ~ 650 $e^- Å^{-2} s^{-1}$). (a) HAADF image of a representative frame from video S1. (b) Enlarged HAADF image of the region enclosed by the yellow square in (a), defined as the initial frame at the very beginning of irradiation (0 s). Time-lapse HAADF images showing nanoparticle evolution at (c) 0 s, (d) 0.8 s, (e) 1.6 s, (f) 2.4 s, (g) 3.2 s, (h) 4.0 s, (i) 4.8 s, and (j) 13.0 s. (k) Time-dependent evolution of the horizontal and vertical distances between the apexes of particles A and B in (b). (l) Intensity profiles along the purple dashed lines in the time-lapse HAADF images.

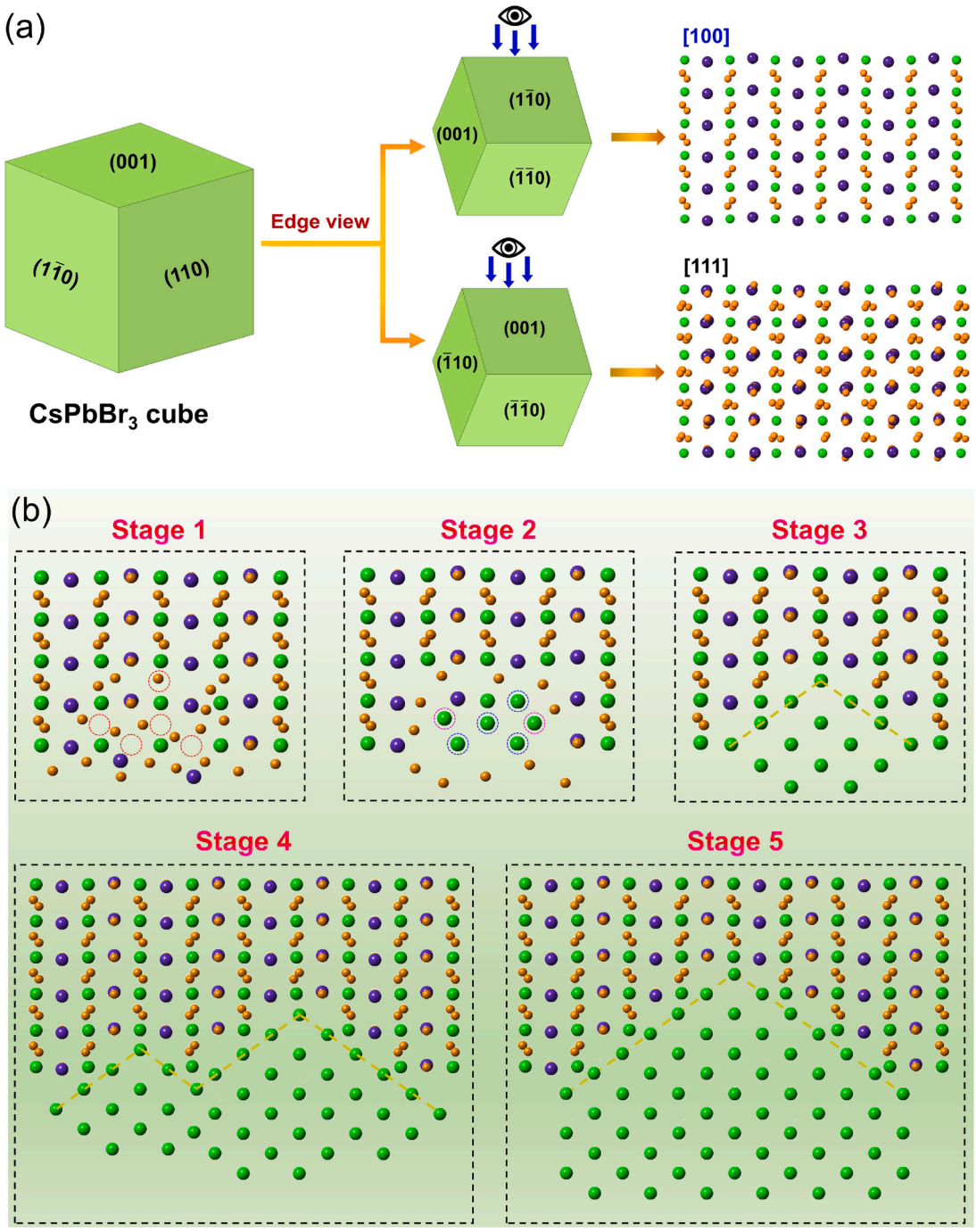

Fig. 7. Schematic illustration of degradation mechanism for the orthorhombic $CsPbBr_3$ under electron-beam irradiation. (a) Edge views of $CsPbBr_3$ cube along [100] and [111] directions. (b) Sequential stages of the degradation process of $CsPbBr_3$ under electron-beam irradiation, viewed along the [100] direction.

Pb atoms exhibit the highest defect formation energy, indicating greater stability within the lattice compared to Cs and Br atoms. However, Br atoms, having the lowest atomic mass, are more susceptible to electron-beam bombardment. Consequently, during the electron-beam irradiation, Br and Cs atoms detach first from the $CsPbBr_3$ lattice, creating vacancies that facilitate the diffusion of Pb atoms. This can explain why the Pb atoms marked by the white and yellow circles in Fig. 5b, c, e and f occupy positions previously occupied by Cs and Br atoms in the $CsPbBr_3$ lattice, leading to the observed unique interface structure in which the outermost layer of the $CsPbBr_3$ consists of Pb atoms.

To directly observe the degradation process of $CsPbBr_3$ particles, extensive *in-situ* STEM observations were conducted (Video S1, Supporting Information, SI). The video reveals that nucleated Pb nanoparticles undergo layer-by-layer endotaxial growth, followed by coalescence through twinning under continuous electron-beam irradiation. For detailed analysis, a representative frame from Video S1 was selected, as shown in Fig. 6a. Fig. 6b represents an enlarged HAADF image of the region enclosed by the yellow square in Fig. 6a, where two Pb nanoparticles, labeled A and B, are clearly observed. Video S1 shows that nanoparticle A grows layer by layer, while nanoparticle B gradually fuses into A. The layer difference between the outermost Pb layers of nanoparticles A and B is used as a marker for the growth rate of Pb nanoparticle A. In Fig. 6b, this layer difference is 8 layers, which is defined as the initial frame at the very beginning of irradiation (Fig. 6c). As irradiation continues, as shown in Fig. 6c-g, nanoparticle A grows one

layer every 0.8 s. From Fig. 6g to 6i, the growth rate increases to two layers every 0.8 s, indicating that the coalescence rate accelerates as the size difference between nanoparticles A and B increases.

The temporal evolution of the horizontal distance (blue lines in Fig. 6c-h) and vertical distance (red lines in Fig. 6c-h) between the apexes of nanoparticles A and B is plotted in Fig. 6k, providing a quantitative visualization of the coalescence dynamics. After 13 s of irradiation, the coalescence process ceases and the shape of Pb nanoparticle A stabilizes (Fig. 6j).

Intensity profiles surrounding the Pb nanoparticles (Fig. 6l) show that as coalescence proceeds, the image intensity increases and becomes stronger in the middle part of the profile, reflecting the thickening of the fused Pb nanoparticle. Simultaneously, the minimum contrast intensity decreases, indicating ongoing decomposition of the surrounding $CsPbBr_3$ lattice, which supplies additional Pb atoms for the endotaxial growth. In addition, twinning *via* {111} planes of Pb nanoparticles is also observed (Fig. S8). These results demonstrate that under electron-beam irradiation, Pb nanoparticle grows layer by layer. When Pb nanoparticles are in close proximity, coalescence occurs *via* {111} twinning, with Pb atoms supplied from the fused nanoparticle and the surrounding $CsPbBr_3$ lattice, until a larger and more stable Pb nanoparticle is produced.

3.3. Degradation mechanism of orthorhombic $CsPbBr_3$ under electron-beam irradiation

Based on the above analysis, a potential degradation mechanism for the orthorhombic $CsPbBr_3$ under electron-beam irradiation is proposed, as depicted in Fig. 7. Fig. 7a shows a typical $CsPbBr_3$ cube, where the termination surfaces consist of two {001} facets and four {110} facets of orthorhombic $CsPbBr_3$, accompanied by distinct orientations of orthorhombic $CsPbBr_3$ observed from two different edge perspectives. The edge between two {110} facets yields the [100] zone-axis, while the edge between the {001} and {110} facets corresponds to the [111] zone-axis. Because the degradation behaviors along the [100] and [111] zone-axes of orthorhombic $CsPbBr_3$ are very similar, only the [100] zone-axis is discussed as an example.

When an edge of the $CsPbBr_3$ cube is exposed to electron-beam irradiation, the combined effects of electron beam bombardment and irradiation-induced heating induce to the successive detachments of Br and Cs atoms from their lattice sites (Stage 1 in Fig. 7b). These atoms diffuse outward, resulting in Cs and Br vacancies (highlighted by the red circles). It should be noted that a significant number of Br vacancies already exists on the surfaces of $CsPbBr_3$ particles prior to irradiation, which facilitates Pb nanoparticle formation [31]. Subsequently, Pb atoms detach from lattice sites and aggregate by occupying Br and Cs vacancies (blue circles) and interstitial sites (pink circles), as shown by the Stage 2 in Fig. 7b The detailed nucleation mechanism can be found in our previous work [16] Once nucleation conditions are met, Pb nanoparticles and $CsPbBr_3$ lattice form special orientation relationships (Stage 3 in Fig. 7b). As irradiation continues, Pb nanoparticle grows layer by layer. When nearby Pb nanoparticles are sufficiently close, they coalesce through {111} twinning (Stage 4 in Fig. 7b), forming larger Pb nanoparticles. Once the irradiated $CsPbBr_3$ lattice is fully decomposed, the growth and coalescence processes stop, and the Pb nanoparticles stabilize in shape (Stage 5 in Fig. 7b), as observed in Fig. 6j.

4. Conclusions

In summary, orthorhombic $CsPbBr_3$ nanocrystals have been successfully synthesized using a room-temperature SR method. Atomic-resolution STEM imaging reveals that the exposed surfaces of the $CsPbBr_3$ nanocrystals correspond to the {001} and {110} planes. Extensive *in-situ* STEM observations from the edge-view imaging geometry are performed to investigate the growth mechanism of Pb nanoparticles during the degradation of $CsPbBr_3$ nanocrystals under electron-beam irradiation was investigated using *in-situ* STEM and supported by DFT calculations. The results show that the {111} planes of Pb align parallel to the {022} and {202} planes of $CsPbBr_3$, with Pb atomic layers forming an interface between $CsPbBr_3$ and Pb. Furthermore, the Pb nanoparticles exhibit an endotaxial growth mode along the ⟨111⟩ direction. DFT calculations further corroborate this oriented growth and clarify the atomic interface structure to stabilize this process. These findings provide detailed insights into the degradation pathways of all-inorganic metal halide perovskites under electron-beam irradiation, offering a fundamental atomistic understanding that is essential for the future design of irradiation-resistant perovskite-based optoelectronics.

CRediT authorship contribution statement

Qingye Zhang: Writing – original draft, Investigation, Data curation. **Feiyu Diao:** Writing – review & editing, Methodology, Data curation. **Rongsheng Cai:** Investigation, Data curation. **Guangwen Zhou:** Writing – review & editing, Methodology. **Yiqian Wang:** Writing – review & editing, Validation, Supervision, Project administration, Methodology, Funding acquisition.

Declaration of competing interest

The authors declare that they have no known competing financial interests or personal relationships that could have appeared to influence the work reported in this paper.

Acknowledgements

Y.Q. Wang would like to thank the financial support from Shandong Province “Double-Hundred Talent Plan” (Grant No.: WST2018006), the Taishan Scholar Program of Shandong Province, China, and Qingdao International Center of Semiconductor Photoelectric Nanomaterials.

Supplementary materials

Supplementary material associated with this article can be found, in the online version, at doi:10.1016/j.actamat.2026.122070.

References

[1] A.M. Oddo, D. Chabeda, J. Basu, M. Arnold, C. Song, E. Rabani, P. Yang, Exploring the structural origins of optically efficient one-dimensional lead halide perovskite nanostructures, J. Am. Chem. Soc. 147 (2025) 10466–10474.
[2] X. Dong, X. Li, X. Wang, Y. Zhao, W. Song, F. Wang, S. Xu, Z. Miao, Z. Wu, Improve the charge carrier transporting in two-dimensional ruddlesden–popper perovskite solar cells, Adv. Mater. 36 (2024) 2313056. /1–26.
[3] X. Sun, G. Zhang, W. Ma, Y. Hua, H. Liu, J. Liu, Z. Yue, X. Wang, J. Song, X. Tao, Growth of two-inch perovskite $CsPbBr_3$ single-crystal with high irradiation resistance for X-ray detection, Adv. Mater. (2025) e12788. /1-10.
[4] P. Ramasamy, D.-H. Lim, B. Kim, S.-H. Lee, M.-S. Lee, J.-S. Lee, All-inorganic cesium lead halide perovskite nanocrystals for photodetector applications, Chem. Commun. 52 (2016) 2067–2070.
[5] M. Yuan, J. Feng, H. Li, H. Gao, Y. Qiu, L. Jiang, Y. Wu, Remote epitaxial crystalline perovskites for ultrahigh-resolution micro-LED displays, Nat. Nanotechnol. 20 (2025) 381–387.
[6] T. Cai, J. Wang, W. Li, K. Hills-Kimball, H. Yang, Y. Nagaoka, Y. Yuan, R. Zia, O. Chen, Mn^{2+}/Yb^{3+} codoped $CsPbCl_3$ perovskite nanocrystals with triple-wavelength emission for luminescent solar concentrators, Adv. Sci. 7 (2020) 2001317. /1–9.
[7] F. Palazon, Q.A. Akkerman, M. Prato, L. Manna, X-ray lithography on perovskite nanocrystals films: from patterning with anion-exchange reactions to enhanced stability in air and water, ACS Nano 10 (2016) 1224–1230.
[8] S. Huang, Z. Li, B. Wang, N. Zhu, C. Zhang, L. Kong, Q. Zhang, A. Shan, L. Li, Morphology evolution and degradation of $CsPbBr_3$ nanocrystals under blue light-emitting diode illumination, ACS Appl. Mater. Interfaces 9 (2017) 7249–7258.
[9] J. Wu, J. Tong, Y. Gao, A. Wang, T. Zhang, H. Tan, S. Nie, Z. Deng, Efficient and stable thin-film luminescent solar concentrators enabled by near-infrared emission perovskite nanocrystals, Angew. Chem. Int. Ed. 59 (2020) 7738–7742.
[10] T. Wu, Y. Wang, Z. Dai, D. Cui, T. Wang, X. Meng, E. Bi, X. Yang, L. Han, Efficient and stable $CsPbI_3$ solar cells via regulating lattice distortion with surface organic terminal groups, Adv. Mater. 31 (2019) 1900605. /1–9.

[11] H. Huang, B. Chen, Z. Wang, T.F. Hung, A.S. Susha, H. Zhong, A.L. Rogach, Water resistant $CsPbX_3$ nanocrystals coated with polyhedral oligomeric silsesquioxane and their use as solid state luminophores in all-perovskite white light-emitting devices, Chem. Sci. 7 (2016) 5699–5703.
[12] S. Wang, W. Shen, Y. Chu, W. Zhang, L. Hong, A. Mei, Y. Rong, Y. Tang, Y. Hu, H. Han, Mesoporous-carbon-based fully-printable all-inorganic monoclinic $CsPbBr_3$ perovskite solar cells with ultrastability under high temperature and high humidity, J. Phys. Chem. Lett. 11 (2020) 9689–9695.
[13] Z. Dang, J. Shamsi, F. Palazon, M. Imran, Q.A. Akkerman, S. Park, G. Bertoni, M. Prato, R. Brescia, L. Manna, *In situ* transmission electron microscopy study of electron beam-induced transformations in colloidal cesium lead halide perovskite nanocrystals, ACS Nano 11 (2017) 2124–2132.
[14] M. Zhang, H. Li, Q. Jing, Z. Lu, P. Wang, Atomic characterization of byproduct nanoparticles on cesium lead halide nanocrystals using high-resolution scanning transmission electron microscopy, Crystals 8 (2017) 2. /1-10.
[15] Z. Dang, J. Shamsi, Q.A. Akkerman, M. Imran, G. Bertoni, R. Brescia, L. Manna, Low-temperature electron beam-induced transformations of cesium lead halide perovskite nanocrystals, ACS Omega 2 (2017) 5660–5665.
[16] F. Diao, Q. Zhang, J. Wang, W. Liang, F. Rosei, X. Xue, Y. Wang, Thickness-dependent microstructural evolution of $CsPbBr_3$ nanobricks induced by electron beam irradiation, Small Struct 5 (2024) 2300577. /1–11.
[17] X.-G. Zhou, C.-Q. Yang, X. Sang, W. Li, L. Wang, Z.-W. Yin, J.-R. Han, Y. Li, X. Ke, Z.-Y. Hu, Y.-B. Cheng, G. Van Tendeloo, Probing the electron beam-induced structural evolution of halide perovskite thin films by scanning transmission electron microscopy, J. Phys. Chem. C 125 (2021) 10786–10794.
[18] A. Prabhakaran, Z. Dang, R. Dhall, F. Camerin, S. Marín-Aguilar, B. Dhanabalan, A. Castelli, R. Brescia, L. Manna, M. Dijkstra, M.P. Arciniegas, Real-time *in situ* observation of $CsPbBr_3$ perovskite nanoplatelets transforming into nanosheets, ACS Nano 17 (2023) 13648–13658.
[19] M. Ma, X. Zhang, L. Xu, X. Chen, L. Wang, T. Cheng, F. Wei, J. Yuan, B. Shen, Atomically unraveling the structural evolution of surfaces and interfaces in metal halide perovskite quantum dots, Adv. Mater. 35 (2023) 2300653.
[20] V. Milman, B. Winkler, J.A. White, C.J. Pickard, M.C. Payne, E.V. Akhmatskaya, R. H. Nobes, Electronic structure, properties, and phase stability of inorganic crystals: a pseudopotential plane-wave study, Int. J. Quant. Chem. 77 (2000) 895–910.
[21] J.P. Perdew, K. Burke, M. Ernzerhof, Generalized gradient approximation made simple, Phys. Rev. Lett. 77 (1996) 3865–3868.
[22] J. Liu, X. Zheng, O.F. Mohammed, O.M. Bakr, Self-assembly and regrowth of metal halide perovskite nanocrystals for optoelectronic applications, Acc. Chem. Res. 55 (2022) 262–274.
[23] J. Liu, K. Song, Y. Shin, X. Liu, J. Chen, K.X. Yao, J. Pan, C. Yang, J. Yin, L.-J. Xu, H. Yang, A.M. El-Zohry, B. Xin, S. Mitra, M.N. Hedhili, I.S. Roqan, O. F. Mohammed, Y. Han, O.M. Bakr, Light-induced self-assembly of cubic $CsPbBr_3$ perovskite nanocrystals into nanowires, Chem. Mater. 31 (2019) 6642–6649.
[24] R.K. Behera, S. Bera, N. Pradhan, Hexahedron symmetry and multidirectional facet coupling of orthorhombic $CsPbBr_3$ nanocrystals, ACS Nano 17 (2023) 7007–7016.
[25] S. Wang, J. Yu, M. Zhang, D. Chen, C. Li, R. Chen, G. Jia, A.L. Rogach, X. Yang, Stable, strongly emitting cesium lead bromide perovskite nanorods with high optical gain enabled by an intermediate monomer reservoir synthetic strategy, Nano Lett. 19 (2019) 6315–6322.
[26] Y. Liu, M. Ma, X. Zhang, B. Song, X. Chen, F. Wei, J. Yuan, B. Shen, Atomic imaging of the Pb precipitation in lead-halide perovskites, Small Methods 8 (2024) 2301617.
[27] Z. He, D.J. Smith, P.A. Bennett, Endotaxial silicide nanowires, Phys. Rev. Lett. 93 (2004) 256102.
[28] S. Wang, Y. Guo, X. Du, L. Xiong, Z. Liang, M. Ma, Y. Xie, W. You, Y. Meng, Y. Liu, M. Liu, Preferred crystal plane electrodeposition of aluminum anode with high lattice-matching for long-life aluminum batteries, Nat. Commun. 15 (2024) 6476.
[29] D. Yu, M. Scheffler, First-principles study of low-index surfaces of lead, Phys. Rev. B 70 (2004) 155417.
[30] J. Yin, H. Yang, K. Song, A.M. El-Zohry, Y. Han, O.M. Bakr, J.-L. Brédas, O. F. Mohammed, Point defects and green emission in zero-dimensional perovskites, J. Phys. Chem. Lett. 9 (2018) 5490–5495.
[31] J. Kang, J. Li, S.-H. Wei, Atomic-scale understanding on the physics and control of intrinsic point defects in lead halide perovskites, Appl. Phys. Rev. 8 (2021) 031302. /1–21.